

Position reconstruction and surface background model for the PandaX-4T detector

Zhicheng Qian^a, Linhui Gu^a, Chen Cheng^b, Zihao Bo^a, Wei Chen^a, Xun Chen^{a,c,d,e}, Yunhua Chen^{e,f}, Zhaokan Cheng^g, Xiangyi Cui^c, Yingjie Fan^h, Deqing Fangⁱ, Zhixing Gao^a, Lisheng Geng^{b,j,k,l}, Karl Giboni^{a,e}, Xunan Guo^b, Xuyuan Guo^{e,f}, Zichao Guo^b, Chencheng Han^c, Ke Han^{a,e}, Changda He^a, Jinrong He^f, Di Huang^a, Houqi Huang^m, Junting Huang^{a,e}, Ruquan Hou^{d,e}, Yu Houⁿ, Xiangdong Ji^o, Xiangpan Ji^p, Yonglin Ju^{e,n}, Chenxiang Li^a, Jiafu Li^q, Mingchuan Li^{e,f}, Shuaijie Li^{a,e,f}, Tao Li^g, Zhiyuan Li^g, Qing Lin^{r,s}, Jianglai Liu^{a,c,d,e}, Congcong Luⁿ, Xiaoying Lu^{t,u}, Lingyin Luo^v, Yunyang Luo^s, Wenbo Ma^a, Yugang Maⁱ, Yajun Mao^v, Yue Meng^{a,d,e}, Xuyang Ning^a, Binyu Pang^{t,u}, Ningchun Qi^{e,f}, Xiangxiang Ren^{t,u}, Dong Shan^p, Xiaofeng Shang^a, Xiyuan Shao^p, Guofang Shen^b, Manbin Shen^{e,f}, Wenliang Sun^{e,f}, Yi Tao^w, Anqing Wang^{t,u}, Guanbo Wang^a, Hao Wang^a, Jiamin Wang^c, Lei Wang^x, Meng Wang^{t,u}, Qihong Wangⁱ, Shaobo Wang^{a,e,m}, Siguang Wang^v, Wei Wang^{g,q}, Xiuli Wangⁿ, Xu Wang^c, Zhou Wang^{a,c,d,e}, Yuehuan Wei^g, Weihao Wu^{a,e}, Yuan Wu^a, Mengjiao Xiao^a, Xiang Xiao^q, Kaizhi Xiong^{e,f}, Yifan Xuⁿ, Shunyu Yao^m, Binbin Yan^c, Xiyu Yan^y, Yong Yang^{a,e}, Peihua Ye^a, Chunxu Yu^p, Ying Yuan^a, Zhe Yuanⁱ, Youhui Yun^a, Xinning Zeng^a, Minzhen Zhang^c, Peng Zhang^{e,f}, Shibo Zhang^c, Shu Zhang^q, Tao Zhang^{a,c,d,e}, Wei Zhang^c, Yang Zhang^{t,u}, Yingxin Zhang^{t,u}, Yuanyuan Zhang^c, Li Zhao^{a,c,d,e}, Jifang Zhou^{e,f}, Jiayu Zhou^m, Jiayi Zhou^c, Ning Zhou^{a,c,d,e}, Xiaopeng Zhou^b, Yubo Zhou^a, Zhizhen Zhou^a

^a*School of Physics and Astronomy Shanghai Jiao Tong University Key Laboratory for Particle Astrophysics and Cosmology (MoE) Shanghai Key Laboratory for Particle Physics and Cosmology Shanghai 200240 China*

^b*School of Physics Beihang University Beijing 102206 China*

^c*New Cornerstone Science Laboratory Tsung-Dao Lee Institute Shanghai Jiao Tong University Shanghai 201210 China*

^d*Shanghai Jiao Tong University Sichuan Research Institute Chengdu 610213 China*

^e*Jinping Deep Underground Frontier Science and Dark Matter Key Laboratory of Sichuan Province*

^f*Yalong River Hydropower Development Company Ltd. 288 Shuanglin Road Chengdu 610051 China*

Email addresses: mengyue@sjtu.edu.cn (Yue Meng), taoy57@mail.sysu.edu.cn (Yi Tao), nzhou@sjtu.edu.cn (Ning Zhou)

- ^g*Sino-French Institute of Nuclear Engineering and Technology Sun Yat-Sen University
Zhuhai 519082 China*
- ^h*Department of Physics Yantai University Yantai 264005 China*
- ⁱ*Key Laboratory of Nuclear Physics and Ion-beam Application (MOE) Institute of
Modern Physics Fudan University Shanghai 200433 China*
- ^j*Peng Huanwu Collaborative Center for Research and Education Beihang University
Beijing 100191 China*
- ^k*International Research Center for Nuclei and Particles in the Cosmos “ \mathcal{E} ” Beijing Key
Laboratory of Advanced Nuclear Materials and Physics Beihang University Beijing
100191 China*
- ^l*Southern Center for Nuclear-Science Theory (SCNT) Institute of Modern Physics
Chinese Academy of Sciences Huizhou 516000 China*
- ^m*SJTU Paris Elite Institute of Technology Shanghai Jiao Tong University Shanghai
200240 China*
- ⁿ*School of Mechanical Engineering Shanghai Jiao Tong University Shanghai 200240
China*
- ^o*Department of Physics University of Maryland College Park Maryland 20742 USA*
- ^p*School of Physics Nankai University Tianjin 300071 China*
- ^q*School of Physics Sun Yat-Sen University Guangzhou 510275 China*
- ^r*State Key Laboratory of Particle Detection and Electronics University of Science and
Technology of China Hefei 230026 China*
- ^s*Department of Modern Physics University of Science and Technology of China Hefei
230026 China*
- ^t*Research Center for Particle Science and Technology Institute of Frontier and
Interdisciplinary Science Shandong University Qingdao 266237 Shandong China*
- ^u*Key Laboratory of Particle Physics and Particle Irradiation of Ministry of Education
Shandong University Qingdao 266237 Shandong China*
- ^v*School of Physics Peking University Beijing 100871 China*
- ^w*School of Science Sun Yat-Sen University Shenzhen 518107 China*
- ^x*College of Nuclear Technology and Automation Engineering Chengdu University of
Technology Chengdu 610059 China*
- ^y*School of Physics and Astronomy Sun Yat-Sen University Zhuhai 519082 China*

Abstract

We report the position reconstruction methods and surface background model for the PandaX-4T dark matter direct search experiment. This work develops two position reconstruction algorithms: template matching (TM) method and photon acceptance function (PAF) method. Both methods determine the horizontal position of events based on the light pattern of secondary scintillation collected by the light sensors. After a comprehensive evaluation of

resolution, uniformity, and robustness, the PAF method was selected for position reconstruction, while the TM method was employed for verification. The PAF method achieves a bulk event resolution of 1.0 mm and a surface event resolution of 4.4 mm for a typical $S2$ signal with a bottom charge of 1500 PE (about 14 keV). The uniformity is around 20%. Robustness studies reveal average deviations of 5.1 mm and 8.8 mm for the commissioning run (Run0) and the first science run (Run1), respectively, due to the deactivation of certain PMTs. A data-driven surface background model is developed based on the PAF method. The surface background is estimated to be 0.09 ± 0.06 events for Run0 (0.54 tonne·year) and 0.17 ± 0.11 events for Run1 (1.00 tonne·year).

Keywords: Dual-phase time projection chamber, Xenon detector, Reconstruction, Surface background, Dark matter

1. Introduction

The existence of dark matter (DM) is strongly supported by cosmological and astronomical observations [1], yet its nature remains elusive. The Weakly Interacting Massive Particle (WIMP) has become one of the most competitive candidates for dark matter, as suggested by numerous theories beyond the Standard Model of particle physics [2]. Dark matter direct detection experiments, typically situated deep underground, are designed to be particularly sensitive to dark matter within a mass range from approximately GeV/c^2 to $100 \text{ TeV}/c^2$. In recent years, large-scale liquid xenon time projection chambers (TPCs) have led the way in enhancing detection sensitivity [3, 4, 5, 6]. Recently, the PandaX-4T experiment has reported the dark matter search results of the commissioning run (Run0) and the first science run (Run1) [4]. This work focuses on the position reconstruction and surface background model in PandaX-4T WIMP analysis.

In this work, two horizontal position reconstruction algorithms are developed for the PandaX-4T combined analysis using data of both Run0 and Run1 [3, 4]: the template matching (TM) method and the photon acceptance function (PAF) method. Both methods aim to determine the horizontal scattering position of each event based on the information collected by the top PMT array. The TM method uses a set of templates of light patterns, which are generated by optical simulation, to match the measured light distribution pattern. The PAF method utilizes a model that describes the relation

between the light distribution pattern and the scattering position, enabling it to calculate the position based on the measured light distribution. A more accurate position reconstruction enables the development of a reliable surface background model. Surface background is primarily caused by radioactive isotopes on the surface of PTFE reflectors, such as ^{210}Pb , ^{210}Bi and ^{210}Po . In the energy region of interest (ROI) for WIMP analysis, ^{210}Pb is the dominant contributor. In WIMP analysis, determining the fiducial volume (FV) is critical for suppressing background noise and improving detection sensitivity. To optimize the FV, especially at the side boundary, it is essential to obtain a comprehensive understanding of the surface background event distribution. In this work, a data-driven surface background model is established by utilizing the characteristic peak from the ^{210}Po alpha decay, which reflects the $S2$ features of surface events.

In this paper, the content is organized as follows. Sec. 2 illustrates the geometry of the PandaX-4T detector. Sec. 3 introduces position reconstruction algorithms, including optical simulation, TM and PAF construction methods, and advanced corrections applied in PandaX-4T analysis. Sec. 4 describes the performance of the reconstruction algorithms via various properties, including bulk and surface event resolutions, uniformity, and robustness. Sec. 5 presents a data-driven surface background model based on the previously introduced position reconstruction method and provides the final number of surface background events in PandaX-4T analysis.

2. The PandaX-4T detector

The PandaX-4T detector, with a sensitive target of 3.7 tonnes of liquid xenon, is located in the B2 hall of the newly expanded CJPL-II [7, 8]. Schematic diagrams of PandaX-4T detector are shown in figure 1. The central cylindrical TPC has a transverse diameter of 1.2 m and a height of 1.3 m. As shown in figure 1, the TPC is enclosed by highly reflective Polytetrafluoroethylene (PTFE) reflector panels, with 24 wall panels on the side and two panels on the top and bottom. Inside TPC, highly transparent electrodes are designed to generate electric fields. From bottom to top, these include screen mesh, cathode grid, gate mesh, and anode mesh, with separations of 1185 mm and 10 mm, respectively (figure 1b). The gas-liquid interface is between the anode and the gate. Additionally, approximately 60 copper shaping rings, consisting of copper strips arranged in a circular configuration outside the PTFE wall panels as shown in figure 1a, surround

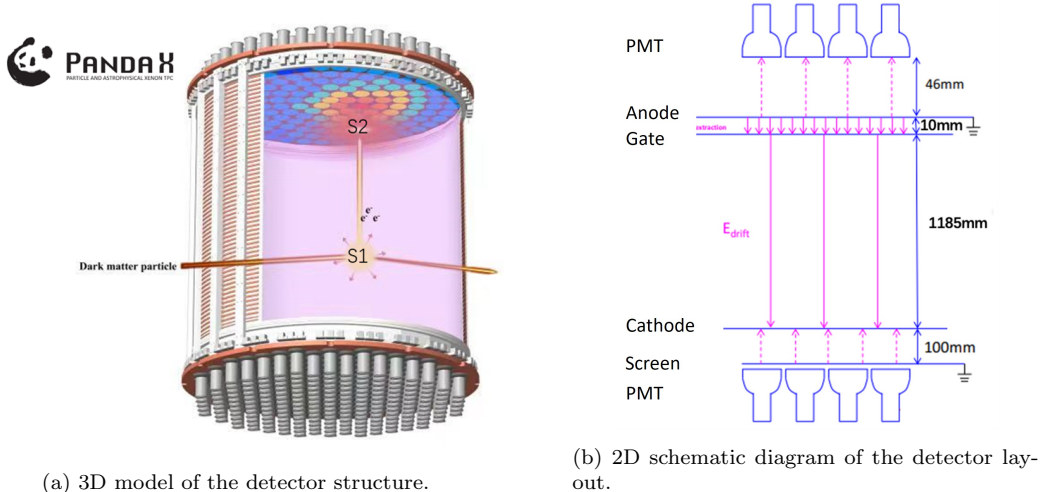


Figure 1: Overview of the PandaX-4T detector design.

the TPC. These rings are designed to maintain a uniform vertical drift field within the detector. Two arrays of Hamamatsu R11410-23 three-inch photo-multipliers (PMTs) are located at the top and bottom of the TPC to collect light signals. The PMTs are fixed onto the copper plates outside the Teflon reflector panels at both ends.

When a WIMP collides with a xenon atom, it generates a prompt scintillation light signal ($S1$) and ionizes electrons. These electrons, driven by the vertical electric field, drift upwards, undergo electroluminescence amplification, and produce a secondary signal ($S2$) that retains the horizontal position of the initial scattering event. These $S1$ and $S2$ signals are collected by the PMT arrays. The scattering vertex in three-dimensions can then be reconstructed based on the collected photon distribution pattern (light pattern) on the top PMT array and the time difference between the $S1$ and $S2$ signals. The reconstruction of the three-dimensional spatial position information of scattering events plays a crucial role in event identification, background suppression, and energy reconstruction.

Currently, the PandaX-4T experiment includes Run0 data with an exposure of 0.54 tonne-year and Run1 data with an exposure of 1.00 tonne-year [4]. Figure 2 shows the distribution and operation status of the top PMT array during the PandaX-4T data-taking process. There are 169 top PMTs placed in a concentric circular pattern. For clarification, the origin of the Carte-

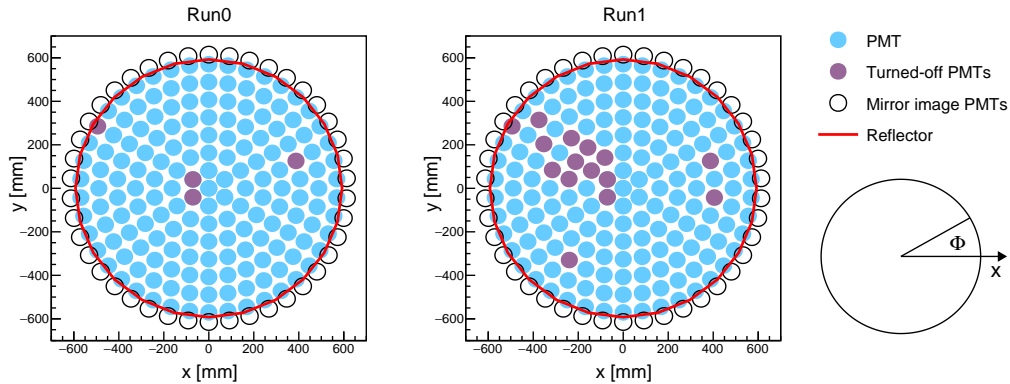


Figure 2: Operation status of top PMT arrays for Run0 (left) and Run1 (right). Different markers indicate the status of the PMTs: blue circles represent operational PMTs, purple circles denote turned-off PMTs, and hollow circles represent image PMTs constructed in the PAF method. The corresponding polar coordinates are shown in the bottom-right corner.

sian coordinate system is defined at the center of the TPC, indicating the z -positions of the gate and cathode are 592.5 mm and -592.5 mm, respectively. For the polar coordinate system, the azimuthal angle (Φ) is defined with the positive x -axis as the zero point.

3. Position reconstruction algorithms

In addition to the conventional reconstruction method known as center of gravity (COG), PandaX-4T used TM and PAF methods to enhance position reconstruction performance.

3.1. Template matching method

The TM method is developed based on optical simulation [9]. The simulated light patterns of top PMT array are used to reconstruct the horizontal position of each signal. To ensure reconstruction accuracy, it is crucial that the simulated light patterns closely match those obtained from actual data. The optical simulation for PandaX-4T is carried out using BambooMC [10], a GEANT4-based Monte Carlo (MC) package. The geometry of the PandaX-4T detector described in Sec. 2 is established in BambooMC.

To more accurately simulate the behavior of the detector, especially the light patterns of the PMTs, tuning to certain parameters of the optical simulation is required, including the reflectivity and refractive index of the PTFE

reflectors, etc. Root mean square (RMS) can serve as a metric to quantify the spreading in a pattern's distribution, which is defined as

$$\text{RMS} = \sqrt{\frac{\sum_i |\vec{r}_i - \vec{r}|^2 \cdot Q_i}{\sum_i Q_i}}, \quad (1)$$

where Q_i is the charge received by the i^{th} PMT, \vec{r}_i is the position of the i^{th} PMT, and \vec{r} is the position of certain event. In simulation, \vec{r} represents the location where the photon is generated, whereas in the data, \vec{r} denotes the reconstructed position of an event.

^{83m}Kr calibration events with 41.5 keV energy peak can be used as a sample for refining simulation parameters. Using the $S2$ distribution of ^{83m}Kr events as input, the simulation parameters are adjusted to match the RMS distributions between the simulation and the data. Figure 3 shows the RMS comparison, with the mean values for the data and the simulation being 217 ± 21 and 215 ± 18 , respectively. The difference of approximately 1% indicates good consistency. The reflectivity and refractive indexes of PTFE are set to be 99% and 1.61 separately. Other optical parameters are summarized in table 1.

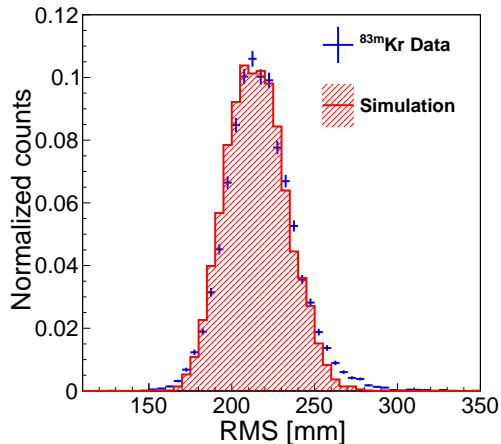


Figure 3: RMS comparison between data and simulation.

Based on optical simulations, about 10^4 templates are generated. Each template represents the expected distribution of light on the top PMT array with a given event position. The horizontal position of each signal is reconstructed by matching its $S2$ light pattern against the generated templates.

Part	Absorption length	Refractivity	Rayleigh scattering length
Gas xenon	100.0 m	1.00	100.0 m
Liquid xenon	10.0 m	1.61	50.0 cm
Anode	0.1255 cm	1.00	/
Gate & screen	0.134 cm	1.61	/
Cathode	0.35 cm	1.61	/

Table 1: Optical properties of major materials involved in simulation.

The maximum likelihood (ML) estimation is used to assess how well the template matches the real light pattern. The position of the template with maximum likelihood most closely approximates the actual scattering point of an event. The likelihood function used in the TM method is expressed as

$$L(\vec{r}_t) = \prod_{i=1}^m p(n_i, p_i) = \prod_{i=1}^m \frac{e^{-Np_i} (Np_i)^{n_i}}{n_i!}, \quad (2)$$

where p_i is the probability of a photoelectron (PE) being detected by the i^{th} PMT for the template generated at position \vec{r}_t , n_i is the number of PEs detected by the i^{th} PMT, $N = \sum_{i=1}^m n_i$ is the total number of PEs and m is the number of all operational top PMTs. In order to efficiently find the best-matched template, the stochastic gradient descent algorithm [11] instead of iterating over all templates is applied. A 10 mm spacing between template positions is selected to strike a balance between computation time and reconstruction resolution.

The final reconstructed position is obtained by performing a weighted average of the template with the maximum likelihood and its surrounding templates:

$$\vec{r}_{\text{reco}} = \frac{\sum_j w_j \cdot \vec{r}_{t,j}}{\sum_j w_j}, \quad w_j = \frac{\ln L_j}{\ln(L_j/L_{\text{max}}) \cdot |\vec{r}_j - \vec{r}_{\text{max}}|}, \quad (3)$$

where L_j and \vec{r}_j are the likelihood value and position of a surrounding template j , while L_{max} and \vec{r}_{max} are that of the best-matched template. The surrounding templates are within a radius of 15 mm around the best-matched template.

3.2. Photon acceptance function method

The PAF method describes the fraction of light that is collected by each PMT as a function of the event's position [12, 13, 14, 15, 16, 17]. This concept has been used to develop algorithms for position reconstruction in scintillation detectors [13]. The light fraction of each PMT is calibrated by optical simulations mentioned in Sec. 3.1.

The single-variable PAF used in this work is similar to that used in PandaX-II [18]. The basic analytical form η_i^0 of the PAF is given by [12]

$$\eta_i^0(\ell_i) = A_i \cdot \exp\left(-\frac{a_i \cdot \frac{\ell_i}{r_i}}{1 + \left(\frac{\ell_i}{r_i}\right)^{1-\alpha_i}} - \frac{b_i}{1 + \left(\frac{\ell_i}{r_i}\right)^{\alpha_i}}\right), \quad (4)$$

where i is the PMT index, and ℓ_i is the distance from the scattering point to the center of the i^{th} PMT. The other parameters, including A_i , α_i , r_i , a_i , b_i , are fitting parameters.

In order to correct the asymmetry caused by PTFE reflection at the border, the concept of ‘‘mirror image PMTs’’ (figure 2) is introduced. η_i^0 is separated into two parts, the reduced object η_i , and the corresponding image, $\eta_{i,im}$. For PandaX-4T analysis, the PAF is extended to

$$\eta_i(\ell_i) = \frac{1}{1 + \omega} \cdot (1 - \rho) \cdot \eta_i^0(\ell_i), \text{ and} \quad (5)$$

$$\eta_{i,im}(\ell_{i,im}) = \omega \cdot \eta_i(\ell_{i,im}), \quad (6)$$

where the factor $\frac{1}{1+\omega}$ represents the proportion of photons received by the PMT that are attributed to the mirrored PMT. ω is non-trivial for PMTs near the boundary and zero for the inner PMTs. The term ρ serves as a correction factor for the global reflection effects. The minus sign before ρ in Eq. 5 represents a cut-off correction. The statistical inference of the position is also done by ML estimation as deduced in the literature [13]. The modified likelihood function considering image PMTs is expressed as

$$\begin{aligned} \ln L(\vec{r}) = & \sum_{\text{edge}} \left(\frac{1}{1 + \omega} \cdot q_i \cdot \ln \frac{\eta_i(\ell_i)}{P(\vec{r})} + \frac{\omega}{1 + \omega} \cdot q_i \cdot \ln \frac{\eta_{i,im}(\ell_{i,im})}{P(\vec{r})} \right) \\ & + \sum_{\text{inner}} q_i \cdot \ln \frac{\eta_i(\ell_i)}{P(\vec{r})}, \end{aligned} \quad (7)$$

where q_i is the collected $S2$ charge by the i^{th} PMT, and the probability $P(\vec{r}) = \sum_i (\eta_i + \eta_{i,im})$. The position with the maximum likelihood, obtained by scanning (x, y) for each event with a step size of 0.01 mm, is taken as the reconstructed position of the event.

3.3. Advanced corrections

Two advanced corrections are applied to the algorithms: partial waveform reconstruction (PWR) and geometric position correction (GPC). The PWR is designed to address light pattern dispersion caused by the tailing of $S2$ signals, which leads to deviations in reconstructed positions. These tails may consist of additional noise charges that do not originate from the $S2$ signals themselves. Possible sources of noise charges include secondary electron signals generated by photoionization and PMT afterpulses. For each signal, instead of the total waveform, PWR reconstructs the position using a waveform segment, selected based on the cumulative distribution function (CDF). Given the signal tailing, the segment's endpoint is set where $\text{CDF} \leq 50\%$, meaning that the first half of the waveform contributes most to the reconstruction. To quantify the effect of different CDF ranges, surface event resolution is measured using the width of the ^{210}Po characteristic Gaussian peak. Figure 4 illustrates the performance across various CDF ranges. For comparison, a “pre-peak” curve is shown, which integrates the waveform from the starting point up to its peak. Optimal performance is achieved when the CDF range is set between 0% and 50%. Notably, the surface event resolution is evaluated as a function of $S2$ bottom charge (Q_{S2_b}), since $S2$ top charge (Q_{S2_t}) may underestimate the true charge due to saturation effects in the top PMTs, making Q_{S2_b} a more reliable choice. The ratio of the top charge to the bottom charge is approximately 4:1 when the PMTs are not saturated.

In both Run0 and Run1, a phenomenon is observed where events at the edge exhibit a noticeable deviation of the reconstructed radial position R towards the center of TPC at 15° and -90° (figure 5). This inward shift becomes more pronounced for events closer to the bottom of the TPC. This may be due to the non-uniformity of the local drift electric field yet no obvious deformations of the reflectors were observed. To more accurately approximate the true positions, GPC is performed. ^{210}Po alpha events, primarily originating from the PTFE surface, are used as samples to eliminate Φ dependence. Additionally, ^{83m}Kr events, which are expected to be uniformly distributed in TPC, are used as samples to align the reconstructed positions

with the geometric positions. Figure 5 demonstrates the effects of GPC at different vertical positions.

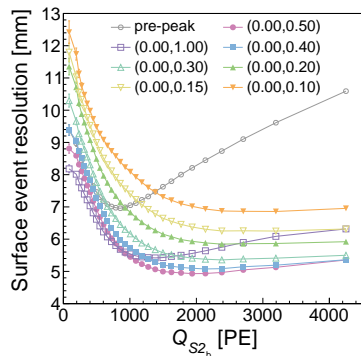


Figure 4: Surface event resolutions for different CDF ranges.

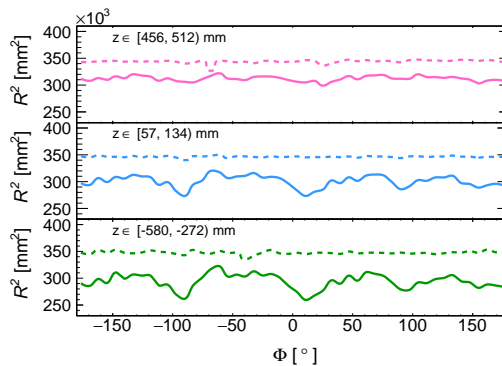


Figure 5: Azimuthal angle distribution of surface events at different vertical positions. (solid lines: before GPC; dashed lines: after GPC)

4. Position reconstruction performance

In this section, the performance of different position reconstruction algorithms will be examined in terms of resolutions, uniformity and robustness.

4.1. Resolutions

Since the reconstructed positions of surface events tend to be more inward than expected, resulting in a larger discrepancy compared to bulk events, the resolutions of bulk and surface events are estimated separately. Bulk event resolution is estimated based on simulations. By using the patterns obtained from simulations as inputs for the reconstruction algorithms, the resolution of bulk events can be evaluated through the discrepancy between the reconstructed positions and the primary positions in MC. The primary positions are set to be within 400 mm from the center of TPC. As illustrated in figure 6, there is a significant enhancement in the bulk resolution of both the PAF and TM methods comparing to the COG method. Within this comparison, the PAF method provides a better performance over TM. Moreover, PAF method depends on physical model, which is more likely to describe the real physical process. Under the circumstances of high photon signal noises, PAF can more accurately reflect the spatial distribution of the photon signal, thereby

avoiding the trap of local optima. Therefore, the position-related analysis are carried out using PAF method, while TM provides a supplementary verification. For clarity, in the following discussion, only the results obtained by the PAF method will be presented.

The position of surface events are expected to be reconstructed at the edge of the TPC. ^{210}Po events, characterized by an alpha decay with energy of 5.3 MeV, are utilized to assess the surface resolution by evaluating the standard deviation of their radial distributions. The ionization electron clouds of surface events may touch the reflector during the drift process, causing some of the ionization electrons to be adsorbed. This results in a suppressed $S2$ signal. Utilizing this feature, resolution in terms of different $S2$ charge can be evaluated, as shown in figure 7. As mentioned before in Sec.3.3, the surface resolution is estimated based on $S2$ bottom charge. From the five curves representing different vertical positions, it can be observed that the closer to the liquid surface, the better the reconstructed resolution. For signals with a small charge, the light pattern tends to be more diffused, making accurate reconstruction more difficult. Conversely, for signals with larger charges, the resolution degrades as the PMTs may become saturated.

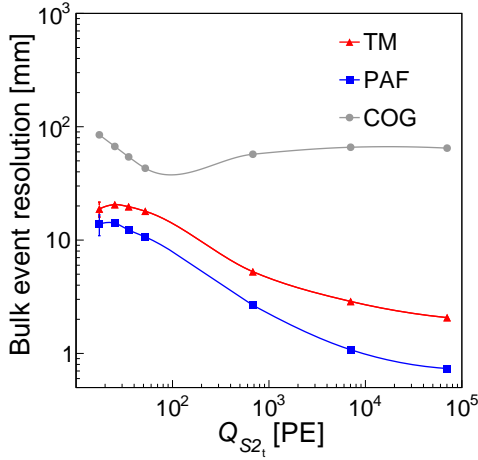


Figure 6: Bulk event resolution on $S2$ top charge (Q_{S2_t}) for different reconstruction methods.

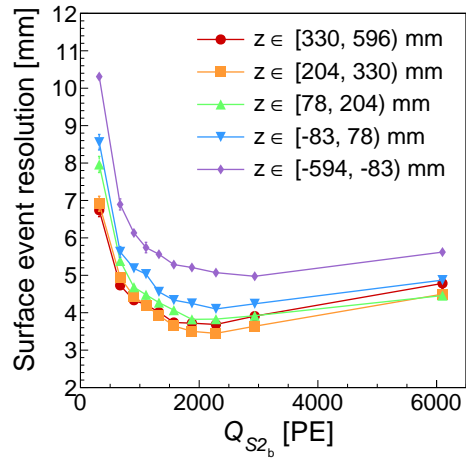


Figure 7: Surface event resolution on $S2$ bottom charge (Q_{S2_b}) at different vertical positions

4.2. Uniformity

During data processing, calibrations are done to help us understand the response of the detector. Calibration sources such as ^{83m}Kr , ^{220}Rn are supposed to be uniformly-distributed. Thus, the normalized spatial distribution $P(r^2)$ of these events can be used to evaluate the performance of position reconstruction. The uniformity can be quantified by relative standard deviation (RSD) after binning, which is defined as

$$\text{RSD} = \frac{\sqrt{\overline{P(n)^2} - [\overline{P(n)}]^2}}{\overline{P(n)}}, \text{ where } \overline{P(n)} = \frac{\sum_{n=0}^{n_{\text{crit}}} P(n)}{n_{\text{crit}}}, \quad \overline{P(n)^2} = \frac{\sum_{n=0}^{n_{\text{crit}}} P(n)^2}{n_{\text{crit}}}, \quad (8)$$

n is the bin index, and n_{crit} corresponds to the bin where the normalized distribution falls to 20% of its maximum value ($P(n_{\text{crit}}) = 0.2 \cdot P_{\text{max}}$). Figure 8 shows the radial distribution of ^{83m}Kr , ^{220}Rn using different reconstruction methods. Along the R^2 axis, from 0 to 0.36 m^2 , the range is divided into

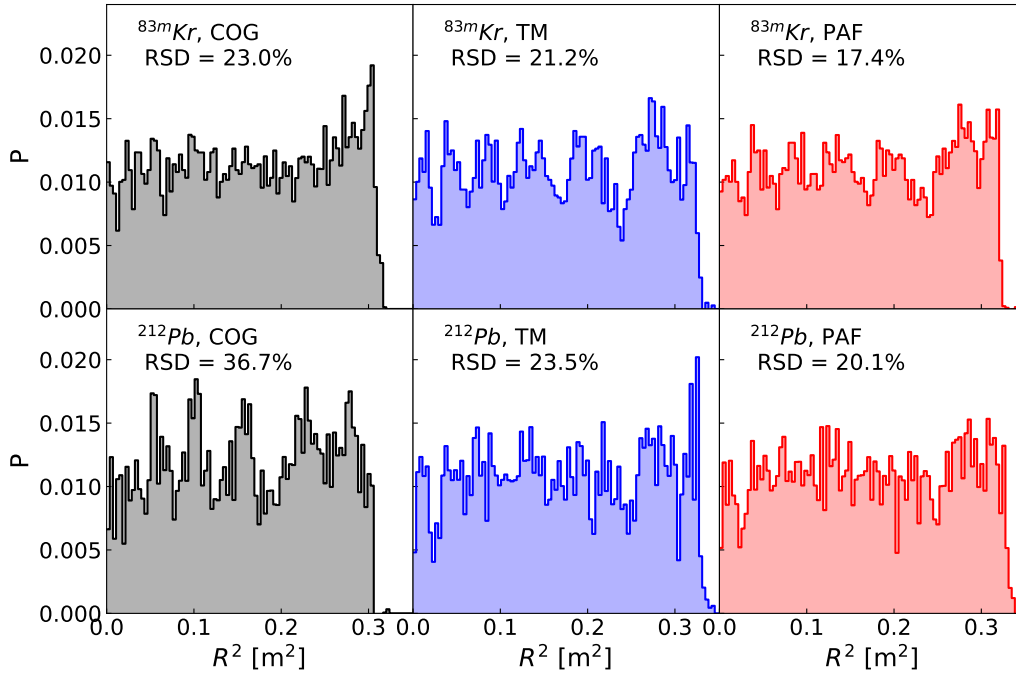


Figure 8: R^2 distribution of ^{83m}Kr (top) and ^{212}Pb (bottom) using different type of reconstruction methods.

100 bins. To ensure comparability between different methods, we averaged and standardized that $n_{\text{crit}} = 90$. Correspondingly, the RSD quantifies the uniformity using data within $R^2 < 0.324 \text{ m}^2$. The PAF method has the minimum RSD among all the three methods, indicating its best performance.

4.3. Robustness

Robustness in position reconstruction refers to the accuracy and reliability of the reconstruction despite missing or degraded data, such as when certain PMTs fail to collect light signals. It quantifies the reconstruction deviation under these compromised conditions. During the data-taking process, four top PMTs in Run0 and additional eleven PMTs in Run1 were turned off individually (figure 2), presenting a challenge for position reconstruction. Robustness is assessed using MC simulations by uniformly scattering points in the $x - y$ plane and comparing primary and reconstructed positions. The saturation effect of the top PMTs is not considered in simulation. Figure 9 shows the deviations at $Q_{S2_t} = 6000 \text{ PE}$ using PAF method under the running conditions of Run0 and Run1. It can be obviously observed that the reconstructed positions show greater deviations around the off-PMT regions (red solid lines in figure 9). To further clarify the robustness, we calculate the average deviation within the off-PMT regions. Figure 10 shows the dependence of robustness on charge, with the PAF method outperforming the TM method in the low-energy region. For a typical $S2_t$ signal at 6000 PE, the

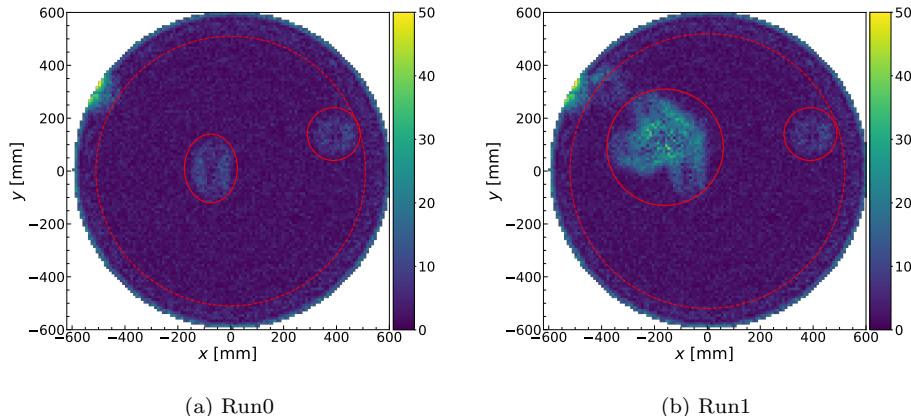


Figure 9: Robustness assessment using MC at $Q_{S2_t} = 6000 \text{ PE}$. The color indicates the deviation at each position. Solid lines represent the off-PMT regions and dashed lines denote the FV boundaries.

mean deviations within the off-PMT regions are 5.1 (3.4) mm and 8.8 (4.6) mm for Run0 and Run1 using PAF (TM) method, respectively. Compared to the situation where the PMTs are in normal operation status (figure 6), the deviation worsens by 1 to 8 mm.

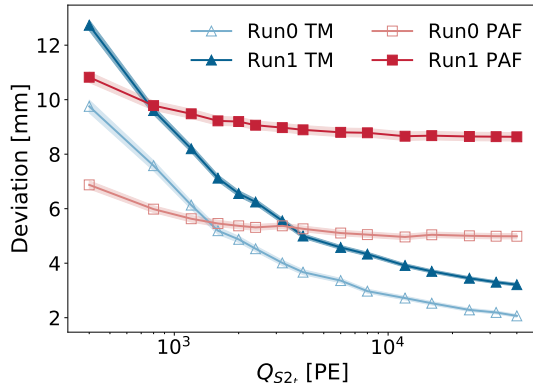


Figure 10: The dependence of deviation on charge in off-PMT regions (The colored bands represent the error bars).

5. Surface background model

To investigate the contribution of surface background events, a surface background model is required to predict the distribution along R and within the parameter space of $\log_{10}(Q_{S2b}/Q_{S1})$ vs. Q_{S1} . This parameter space is used for analyzing WIMP candidates [4]. The model is based on the position reconstruction algorithms discussed in the previous sections. As mentioned in Sec. 4.1, the R distribution of ^{210}Pb can be modeled by studying the $S2$ characteristics of ^{210}Po alpha events, ultimately estimating the number of surface background events within energy ROI and FV. The process of building the surface background model involves the following steps: creating probability density functions (PDFs), 2-D slicing along z and Q_{S2b} , using a re-weighting technique, fittings of model parameters, interpolating along Q_{S2b} , combination and normalization.

Creating PDFs — Assuming that the events in the energy ROI reconstructed outside the PTFE wall originate from the PTFE surface, then the smoothed three-dimensional distribution of $S1$, $S2$, and z from these events can be used as the PDF of the model. Figure 11 demonstrates the PDF and

the bright spot comes from the L-shell Auger electrons and X-ray of ^{210}Pb decay.

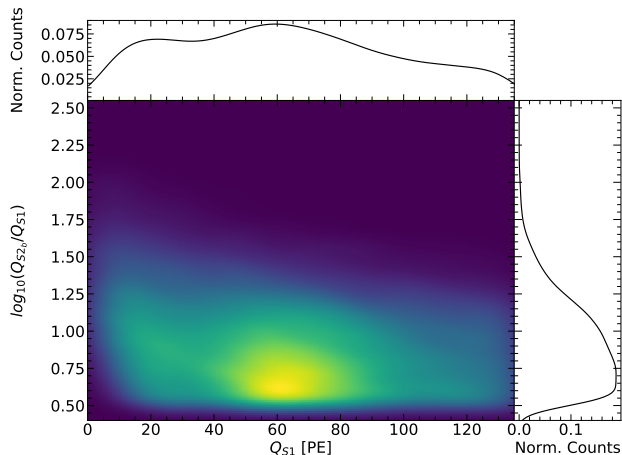


Figure 11: Smoothed distribution of the events outside the PTFE wall in $\log_{10}(Q_{S2_b}/Q_{S1})$ vs. Q_{S1}

2-D slicing along z and Q_{S2_b} — The radial distribution of surface events depends on $S2_b$ charges and vertical position (figure 12a and figure 12b). With GPC mentioned in Sec. 3.3, the radial dependence on Φ has been eliminated, but their PDFs are not uniform (figure 12c). Therefore, a two-dimensional slicing of the ^{210}Po samples in terms of z and $S2$ is performed and the properties of each slice are studied in the $R - \Phi$ plane.

Using a re-weighting technique — When selecting ^{210}Po events as a template, an event whose $S1$ is accidentally paired with a random $S2$ should not be included. For small $S2$, this mis-pairing rate is high. Therefore, a lower threshold for $S2$ has been set to ensure a purer template. Consequently, the $S2$ distribution of the ^{210}Po samples differs from that of low-energy surface background events in the ROI. Using a re-weighting technique, we can better model the distribution of low-energy surface events.

Fittings of model parameters — For each slice, set the median curve in the $R - \Phi$ plane as the zero point. Then, a reduced radial distribution (δR) relative to this median curve can be obtained (figure 13). This distribution is Gaussian-like in shape, and can be fitted using various Gaussian-like functions (table 2) to determine the model parameters such as the center value μ and the standard deviation σ . Figure 13 provides an example slice where the fitting function consists of a Gaussian term and an exponential

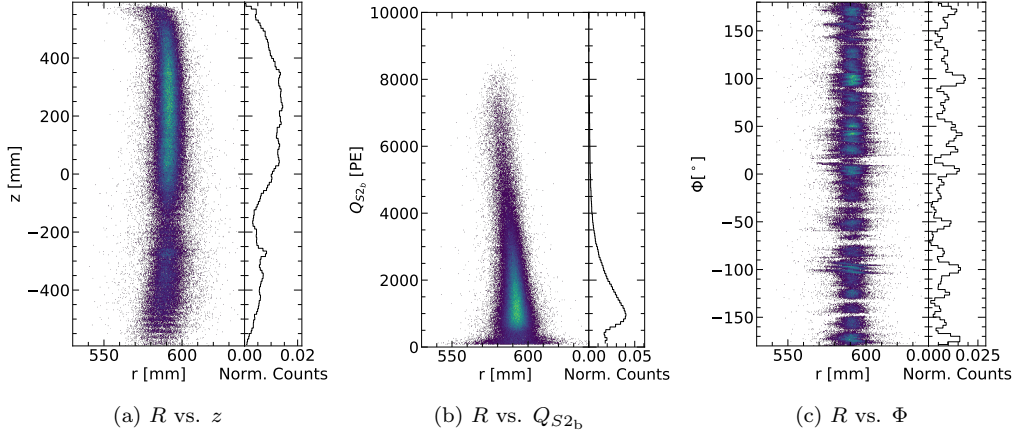


Figure 12: Radial dependence of ^{210}Po surface events on vertical position, $S2_b$ charge and azimuth angle.

term, allowing the derivation of μ, σ and a parameter λ , which describing the decreasing event rate inwards along the radial direction.

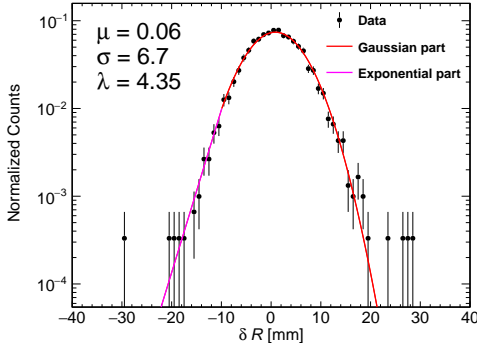


Figure 13: Reduced R distribution relative to the median curve of $R - \Phi$ distribution. Exponential Gaussian tail function is used for fitting, which is composed of a Gaussian term and an exponential term.

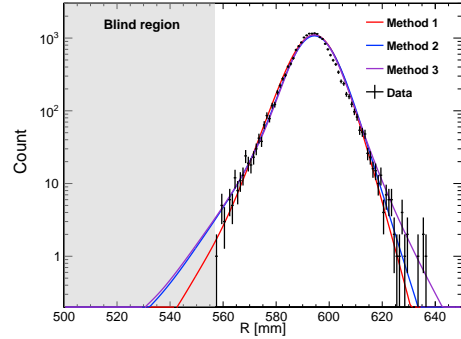


Figure 14: Radial distribution of surface background model using three fitting methods. The corresponding fitting functions are provided in table 2.

Interpolating along Q_{S2_b} — By combining the fitting results of each (z, Q_{S2_b}) slice, we can determine $S2$ charge-dependent parameters for different vertical positions. For example, figure 7 illustrates the case of the parameter σ . To build a smoother model, we further interpolate along the Q_{S2_b} . Consequently, given any pair of values (z, Q_{S2_b}) , their radial distribution can be

determined.

Combination and normalization — For WIMP analysis, only events below the NR median are considered relevant. By combining all slices within ROI from the PDFs (figure 11) mentioned before, the shape of radial distribution for surface events is established. Normalizations are done according to the low energy events reconstructed outside the PTFE wall. Finally, figure 14 shows the radial distribution of surface background model using different fitting methods provided in table 2. For a blind analysis, we mask the data in the blind region where $R^2 < 0.31 \text{ m}^2$. The consistency between the model and data can be evaluated by the χ^2/NDF value in the region between the blind boundary and the peak (table 2). The models effectively describe the data outside the blind region, enabling estimation of the surface background contribution inside the blind region.

Method	Function	Run0		Run1	
		count	χ^2/NDF	count	χ^2/NDF
1	$f(x) = \begin{cases} A_1 \exp\left(-\frac{(x-\mu)^2}{2\sigma_1^2}\right) & \text{if } x < \mu \\ A_2 \exp\left(-\frac{(x-\mu)^2}{2\sigma_2^2}\right) & \text{if } x \geq \mu \end{cases}$	0.03	2.3	0.05	4.4
2	$f(x) = \begin{cases} A_1 \exp\left(-\frac{(x-\mu)^2}{\lambda}\right) & \text{if } x < \mu - \sigma \\ A_2 \exp\left(-\frac{(x-\mu)^2}{2\sigma^2}\right) & \text{if } x \geq \mu + \sigma \end{cases}$	0.12	2.9	0.26	2.3
3	$f(x) = \begin{cases} A_1 \exp\left(-\frac{(\mu-x)}{\lambda_1}\right) & \text{if } x < \mu - \sigma \\ A_2 \exp\left(-\frac{(x-\mu)^2}{2\sigma^2}\right) & \text{if } \mu - \sigma \leq x \leq \mu + \sigma \\ A_3 \exp\left(-\frac{(x-\mu)}{\lambda_2}\right) & \text{if } x > \mu + \sigma \end{cases}$	0.13	2.3	0.19	2.5
Average		0.09 \pm 0.06		0.17 \pm 0.11	

Table 2: Surface background estimation.

Based on the surface background model and other background sources, FV is optimized utilizing a figure-of-merit [19]. The R^2 boundary is determined to be 0.26 m^2 and 0.27 m^2 [4] for Run0 and Run1 by the dominance of surface background events. The number of surface background events can then be estimated by integrating radially from 0 to the R^2 boundary. Table 2 summarizes the estimation of surface events using three fitting functions. The final result is the average of the three fitting functions, with the error represented by their standard deviations. Figure 15 shows the distribution of surface background events inside FV in the parameter space of $\log_{10}(Q_{S2_b}/Q_{S1})$ vs. Q_{S1} . For WIMP analysis, the energy ROI is defined as $Q_{S1} \in (2, 135)$ PE, below NR median curve and above 99.5% NR acceptance boundary. Within the optimized FV and energy ROI, the surface background is estimated to be 0.09 ± 0.06 events for Run0 and 0.17 ± 0.11 events for Run1, respectively [4].

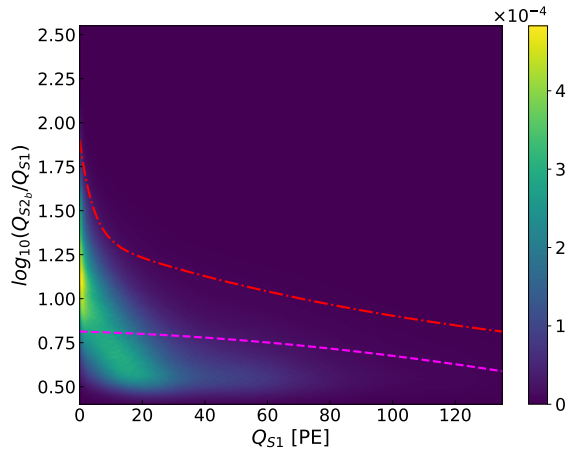


Figure 15: Distribution of surface background events inside FV in $\log_{10}(Q_{S2_b}/Q_{S1})$ vs. Q_{S1} , overlaid with NR median curve (red line) and 99.5% NR acceptance boundary (magenta line)

6. Summary

In summary, we present two position reconstruction algorithms developed for the PandaX-4T experiment. Tailored to the specific characteristics of the PandaX-4T detector, these algorithms include advanced corrections to further enhance reconstruction resolution. After evaluating both methods based on their resolution and uniformity performance, the PAF method was chosen for primary position reconstruction, while the TM method served as a verification tool. For a typical $S2$ signal with $Q_{S2_b} = 1500$ PE (equivalently, $Q_{S2_t} = 6000$ PE), the bulk and surface event resolution reaches approximately 1.0 mm and 4.4 mm. The uniformity is estimated using ^{83m}Kr and ^{212}Pb events, resulting in an RSD of around 20%. The Robustness study indicates that the average deviations are 5.1 mm and 8.8 mm for Run0 and Run1 within off-PMT regions when $Q_{S2_t} = 6000$ PE. The PAF method also forms the basis for a data-driven surface background model, which estimates the surface background contribution as 0.09 ± 0.06 events for Run0 and 0.17 ± 0.11 events for Run1. Beyond enhancing the immediate accuracy of position reconstruction, these improvements contribute significantly to optimizing energy reconstruction, correcting detector non-uniformity, and boosting the signal-to-noise ratio. Looking ahead, these advancements will not only refine background modeling but also improve the overall sensitivity

of the experiment, paving the way for future breakthroughs in dark matter detection.

Acknowledgment

This work has been supported by the Ministry of Science and Technology of China (No. 2023YFA1606204), the National Natural Science Foundation of China (No. 12222505, No. 12205181, No. 12325505). We also thank the sponsorship from the Chinese Academy of Sciences Center for Excellence in Particle Physics (CCEPP), Hongwen Foundation in Hong Kong, New Cornerstone Science Foundation, Tencent Foundation in China, and Yangyang Development Fund.

References

- [1] G. Bertone, D. Hooper, J. Silk, Particle dark matter: evidence, candidates and constraints, *Physics Reports* 405 (5-6) (2005) 279–390. doi:10.1016/j.physrep.2004.08.031.
- [2] J. Billard, et al., Direct Detection of Dark Matter – APPEC Committee Report (4 2021). arXiv:2104.07634.
- [3] Y. Meng, et al., Dark Matter Search Results from the PandaX-4T Commissioning Run, *Phys. Rev. Lett.* 127 (2021) 261802. doi:10.1103/PhysRevLett.127.261802.
- [4] Z. Bo, et al., Dark matter search results from 1.54 Tonne · Year exposure of pandax-4t, *Phys. Rev. Lett.* 134 (2025) 011805. doi:10.1103/PhysRevLett.134.011805.
URL <https://link.aps.org/doi/10.1103/PhysRevLett.134.011805>
- [5] E. Aprile, et al., First dark matter search with nuclear recoils from the XENONnT experiment, *Phys. Rev. Lett.* 131 (4) (2023) 041003. doi:10.1103/PhysRevLett.131.041003.
- [6] J. Aalbers, et al., First dark matter search results from the LUX-ZEPLIN (LZ) experiment, *Phys. Rev. Lett.* 131 (4) (2023) 041002. doi:10.1103/PhysRevLett.131.041002.

- [7] J. Li, et al., The Second-phase Development of the China JinPing Underground Laboratory, *Physics Procedia* 61 (2015) 576–585, 13th International Conference on Topics in Astroparticle and Underground Physics, TAUP 2013. doi:<https://doi.org/10.1016/j.phpro.2014.12.055>.
- [8] K. J. Kang, et al., Status and prospects of a deep underground laboratory in China, *J. Phys. Conf. Ser.* 203 (2010) 012028. doi:[10.1088/1742-6596/203/1/012028](https://doi.org/10.1088/1742-6596/203/1/012028).
- [9] S. Langrock, Energy response and position reconstruction in the DEAP-3600 dark matter experiment, *Journal of Physics: Conference Series* 1342 (2020) 012071. doi:[10.1088/1742-6596/1342/1/012071](https://doi.org/10.1088/1742-6596/1342/1/012071).
- [10] X. Chen, et al., BambooMC — A Geant4-based simulation program for the PandaX experiments, *Journal of Instrumentation* 16 (09) (2021) T09004. doi:[10.1088/1748-0221/16/09/t09004](https://doi.org/10.1088/1748-0221/16/09/t09004).
- [11] S. Ruder, An overview of gradient descent optimization algorithms, *CoRR* abs/1609.04747 (2016). arXiv:[1609.04747](https://arxiv.org/abs/1609.04747).
- [12] V. N. Solovov, et al., Position Reconstruction in a Dual Phase Xenon Scintillation Detector, *IEEE Transactions on Nuclear Science* 59 (6) (2012) 3286–3293. doi:[10.1109/TNS.2012.2221742](https://doi.org/10.1109/TNS.2012.2221742).
- [13] R. M. Gray, A. Macovski, Maximum a Posteriori Estimation of Position in Scintillation Cameras, *IEEE Transactions on Nuclear Science* 23 (1) (1976) 849–852. doi:[10.1109/TNS.1976.4328354](https://doi.org/10.1109/TNS.1976.4328354).
- [14] D. Akerib, et al., Position reconstruction in LUX, *Journal of Instrumentation* 13 (02) (2018) P02001. doi:[10.1088/1748-0221/13/02/P02001](https://doi.org/10.1088/1748-0221/13/02/P02001). URL <https://dx.doi.org/10.1088/1748-0221/13/02/P02001>
- [15] A. Lindote, et al., Preliminary results on position reconstruction for ZEPLIN III, *Nuclear Instruments and Methods in Physics Research Section A: Accelerators, Spectrometers, Detectors and Associated Equipment* 573 (1) (2007) 200–203, proceedings of the 7th International Conference on Position-Sensitive Detectors. doi:<https://doi.org/10.1016/j.nima.2006.10.254>.

- [16] J. P. Brodsky, *xy* Position Reconstruction in DarkSide-50 (1 2015). doi: 10.2172/1212164.
URL <https://www.osti.gov/biblio/1212164>
- [17] E. Aprile, et al., XENON1T dark matter data analysis: Signal reconstruction, calibration, and event selection, Phys. Rev. D 100 (2019) 052014. doi:10.1103/PhysRevD.100.052014.
URL <https://link.aps.org/doi/10.1103/PhysRevD.100.052014>
- [18] D. Zhang, et al., Horizontal position reconstruction in PandaX-II, Journal of Instrumentation 16 (11) (2021) P11040. doi:10.1088/1748-0221/16/11/p11040.
- [19] G. Cowan, Discovery sensitivity for a counting experiment with background uncertainty (2012).